Light-adapted flicker optoretinograms captured with a spatio-temporal optical coherence-tomography (STOC-T) system

SŁAWOMIR TOMCZEWSKI,[1,2,5] PIOTR WĘGRZYN,[1,2,3,5] DAWID BORYCKI,[1,2] EGIDIJUS AUKSORIUS,[1,2,4] MACIEJ WOJTKOWSKI,[1,2] AND ANDREA CURATOLO[1,2,*]

[1] *International Centre for Translational Eye Research, Skierniewicka 10A, 01-230, Warszawa, Poland*
[2] *Institute of Physical Chemistry, Polish Academy of Sciences, Kasprzaka 44/52, 01-224 Warszawa, Poland*
[3] *Faculty of Physics, University of Warsaw, Pasteura 5, 02-093 Warszawa, Poland*
[4] *Center for Physical Sciences and Technology (FTMC), Saulėtekio al. 3, LT-10257 Vilnius, Lithuania*
[5] *Equal contributors.*
[*]acuratolo@ichf.edu.pl

Abstract: For many years electroretinography (ERG) has been used for obtaining information about the retinal physiological function. More recently, a new technique called optoretinography (ORG) has been developed. In one form of this technique, the physiological response of retinal photoreceptors to visible light, resulting in a nanometric photoreceptor optical path length change, is measured by phase-sensitive optical coherence tomography (OCT). To date, a limited number of studies with phase-based ORG measured the retinal response to a flickering light stimulation. In this work, we use a spatio-temporal optical coherence tomography (STOC-T) system to capture optoretinograms with a flickering stimulus over a 1.7×0.85 mm^2 area of a light-adapted retina located between the fovea and the optic nerve. We show that we can detect statistically-significant differences in the photoreceptor optical path length (OPL) modulation amplitudes in response to different flicker frequencies and with better signal to noise ratios (SNRs) than for a dark-adapted eye. We also demonstrate the ability to spatially map such response to a patterned stimulus with light stripes flickering at different frequencies, highlighting the prospect of characterizing the spatially-resolved temporal-frequency response of the retina with ORG.

1. Introduction

For many years visual inspection of fundus photography [1] and examination of images acquired with optical coherence tomography (OCT) [2] have been used by ophthalmologists for eye disease diagnosis and monitoring therapy progress thanks to their ability to detect morphological biomarkers of pathophysiology.

However, imaging morphological manifestation of retinal diseases alone does not provide sufficient information on the loss of functionality of retinal neurons, which, in most cases, lies at the center of the pathophysiology process [3]. Electroretinography (ERG) has been used for measuring the retinal physiological response to light stimulation for many years [4], by recording the electrical currents generated directly by retinal neurons in combination with contributions from retinal glia. The drawback of ERG is that it measures an average response from large portions of the retina, and it might miss physiological changes occurring only in small areas. This issue can be partially solved by multifocal ERG [5] which measures the response from specific retinal regions. Nonetheless, researchers have for decades investigated potential light-evoked optical biomarkers of neural function and dysfunction in the retina, which could give rapid, non-invasive, objective information, complementary to that of electrophysiological methods.

Over ten years ago, it was shown that OCT could detect small changes in infrared (IR) reflected light intensity occurring after simultaneous stimulation with visible light on animal retinas *in vitro* [6,7] and *in vivo* [8]. Around the same time, Jonnal, *et al.,* and Grieve, *et al.*, recorded such reflectance changes *in vivo* from individual photoreceptors using, respectively, a flood-illumination retina camera equipped with adaptive optics [9] and an adaptive optics scanning laser ophthalmoscope [10]. These findings laid the foundations for optoretinography (ORG) [3,11], a wealth of techniques that measure light-evoked intrinsic optical signals [12] from groups or even single photoreceptors. These signals can be derived from intensity-based measurements (iORG) [13] or phase-based optoretinograms (pORG) [14].

A breakthrough in the latter category happened in 2016 when a group from Lübeck used a Full-Field Fourier-Domain OCT system to measure the photoreceptor response to light stimulus in humans *in vivo* [15]. Their results showed that the optical path length (OPL) change in the photoreceptor layer in response to a stimulus consists of two phases: a fast negative OPL change (contraction), which is later followed by a slower positive response of larger amplitude (expansion). Other important ORG results have been obtained with scanning OCT systems, often combined with adaptive optics. In 2017, the slow photoreceptor expansion response was explained, with the help of an iORG system, as a result of water diffusion into the retina outer segment to maintain the osmotic balance during the phototransduction cascade [16]. In 2019, it was shown that it is possible to use cellular-resolution pORG for individual cone classification in humans *in vivo* [17]. The following year a high-speed adaptive optics line-scan OCT system was used for cellular-resolution pORG [18] and additional models explaining the potential origin of both the fast and slow response arose [19–21]. ORG was also used for *in vivo* detection of photoreceptor dysfunction due to retinal degeneration in mice [22,23].

Measurements of the retinal response to a flickering stimulus have been performed with ERG multiple times. They have proven instrumental in the analysis of retinal light adaptation [24] and critical flicker frequency (CFF) variations between the macula and periphery [25]. Despite the additional advantages of ORG, only a limited number of studies of flicker ORG have been reported in the literature to the best of our knowledge. Among those, an iORG study [26] measured the photoreceptor response to a periodic stimulus limited to a single low frequency (5 Hz), while, more recently, two pORG studies [27,28] measured the dark-adapted photoreceptor response in the range between 1 Hz and 6.6 Hz and the inner plexiform layer slow response in the range between 1 Hz and 50 Hz, respectively. However, these studies struggled to measure the fast retinal response at frequencies above 10 Hz.

In this paper, we present the technical developments of a system for flicker ORG under light-adapted conditions that can improve the measurement of the fast response to a flickering stimulation in the frequency range above 10 Hz and spatially map the photoreceptors OPL modulation amplitude in response to these flickering stimuli.

2.   Materials and methods

This section describes the materials and methods used for all ORG experiments. More specifically, Section 2.1 describes the OCT and light stimulation setups. Section 2.2 details the ORG data acquisition and signal processing. In section 2.3, we determine the most suitable adaptation before the flicker stimulus. Section 2.4 then quantifies the system displacement sensitivity and OPL modulation amplitude sensitivity.

2.1.   Spatio-temporal optical coherence tomography (STOC-T) system

In our work, we used a STOC-T setup described in detail by Auksorius *et al*. [29,30]. We employed a wavelength-swept laser (Broadsweeper BS-840-2-HP, Superlum) with a tuning range from 803 nm to 878 nm, operating at a sweeping speed of 14600 nm/s. We provided effective crosstalk reduction [30,31] of scattered light in brightfield images using a 300 m patch cable

of multimode fiber [29,30,32] (FG050LGA, Thorlabs) after the light source. A two-telescope system (L$_1$-L$_2$, L$_3$-L$_8$, where the focal lengths of L$_1$, L$_2$, L$_3$, and L$_8$ equal 11 mm, 50 mm, 100 mm, and 50 mm, respectively) imaged the fiber tip to the front focal plane of the eye with a ~2.3x magnification factor. This provided an IR illumination spot size of ~1.7 mm 1/e^2 diameter on the retina and a power of 3.9 mW.

The visible light stimulus path was made collinear with the IR illumination path by introducing a dichroic mirror between the lens L$_3$ and the beam splitter BS. White light from an LED (MNWHL4, Thorlabs) collimated by an achromatic doublet (L$_9$, with a focal length of 30 mm) and a digital micromirror device (DMD) (v9501, Vialux) provided a variable patterned and flickering light stimulation (20 mm x 10 mm), relayed on the retina by another two-telescope system (L$_{10}$-L$_{11}$, L$_8$-eye optics, where both focal lengths of L$_{10}$ and L$_{11}$ equal 150 mm, and the size of the stimulus on the retina is approximately 9.2 mm x 4.6 mm). A non-flickering fixation target was added to the DMD pattern to control the degree of eccentricity of the stimulated retinal area. Similarly, the fellow eye was provided with a non-flickering laser fixation target only for the control measurements in the dark (without stimulus). We estimated the photon flux (PF_r) on the retina, *i.e.*, the number of photons (energy units) per unit time, per unit area, in Eq. (1) by diving the irradiance (the light energy per unit time, per unit area) by the mean energy of a photon $E_{\overline{ph}}$ of our white light stimulus, *i.e.*,

$$PF_r = \frac{c \cdot P_p}{M^2 \cdot A_{DMD} \cdot E_{\overline{ph}}} \left[\frac{\mu W}{\mu m^2} \frac{n_{\overline{ph}}}{\mu J} = \frac{n_{\overline{ph}}}{\mu m^2 s} \right], \quad (1)$$

where P_p is the optical power of the white LED in front of the eye pupil, M^2 is the square of the magnification $M = 0.46$ between the stimulus (DMD) plane and the retina, A_{DMD} is the area of the DMD stimulus, $E_{\overline{ph}} = 3.6 \cdot 10^{-13}$ μJ is the energy of a photon at the central wavelength, and c is a coefficient estimating all losses of the incident light especially on the iris (where $c \cong 75\%$, as determined by empirical observations during stimulation).

We also worked out the photoreceptor cone bleaching (%) for short bleaching exposures [33,34] after converting the stimulus irradiance on the retina (radiometric quantity) in $\frac{\mu W}{\mu m^2}$ to the retinal illuminance (photometric quantity) in Td [35].

Adjustment of the position of the last lens of the second telescope (L$_8$) in the illumination path, placed after the beam splitter BS, allowed correction of the eye refractive error and simultaneously proper imaging of the retina through another telescope (L$_6$-L$_7$, where both focal lengths of L$_6$ and L$_7$ equal 150 mm) in the detection path on an ultra-fast camera sensor (FastCam SA-Z, Photron).

The reference arm included a two-lens system (L$_4$-L$_5$, where the focal length of L$_4$ is 50 mm and L$_5$ is a Plan Achromat Objective with an effective focal length equal to 18 mm) and a titled mirror providing a slightly off-axis reference reflection for sending the reference beam around the rod mirror and onto the preview camera. The incorporation of an additional detector – a line scan camera (N4K-7-F, Alkeria) – behind the rod mirror and an achromatic doublet (L$_{12}$, with a focal length of 30 mm), enabled real-time axial preview [36] of the retina that facilitated patient's alignment. A schematic of the system is presented in Fig. 1, including the white light stimulus spectrum incident on the eye. For an emmetropic eye, the magnification of the detection path was ~4x. The measured system OCT sensitivity was 69 dB for the ultra-fast camera set at 100 kfps (kilo frames per second).

2.2. ORG data acquisition and processing

To produce a 3-D OCT volume, we acquired sets of 512 images of 512×256 pixels, corresponding to a 1.70×0.85 mm^2 field of view (FOV) on the retina, synchronized with the laser sweep, at a camera shutter speed of 100 kfps (enabling a volume acquisition rate of 100 kfps / 512 fpv = 195.3 Hz, fpv: frames per volume). Figures 2(a)–2(b) show *en-face* and B-scan STOC-T
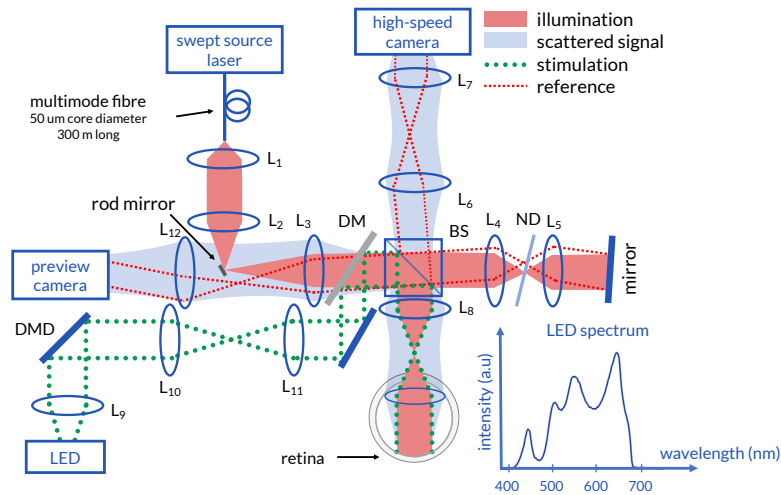
Fig. 1. Schematic of the STOC-T setup with a path for a patterned flickering stimulus (green dotted lines). DMD – digital micromirror device; DM – dichroic mirror, BS – beam splitter, LED – light-emitting diode, L_1-L_{12} – achromatic lenses. The multimode fiber provides effective crosstalk reduction. The retinal and reference mirror planes are conjugated to the high-speed and preview camera, while the DMD plane is conjugated to the retina. The reference mirror is slightly tilted so that the reference beam is not blocked by the pick-off (rod) mirror. The inset shows the white light LED spectrum entering the eye pupil.

images of the retina of a healthy volunteer overlaid onto an IR cSLO fundus image and a clinical SD-OCT B-scan (Spectralis HRA + OCT, Heidelberg Engineering), respectively. Figure 2(c) presents a STOC-T B-scan showing the location of the photoreceptor inner- and outer-segment junction (IS/OS) and the cone outer-segment tips (COST) layers.

For flicker ORG, our protocol included light adaptation for a period of roughly 60 seconds with a pre-flickering stimulus. This, as will become clearer later, was made necessary to detect photoreceptor OPL modulation amplitudes with higher signal-to-noise ratios (SNR). After the pre-flickering phase, we acquired 170 repeated spectral volume recordings every 5.32 ms, for ~0.9 s, with a desired light stimulus spatial and temporal pattern, as depicted in Fig. 3(a). Data processing involved several steps, from generating a complex 3D OCT image from the raw spectral brightfield acquisition to extracting an *en-face* map of the OPL variation over time for the photoreceptor outer segment.

To generate complex OCT images of each volume (Fig. 3(b)), we firstly subtracted the spectrum DC level, estimated by band-pass filtering the interferogram, from the spectral fringe pattern at each pixel location (x, y). Then we applied a Hamming window to the spectra, and we spatially filtered [37] each *en-face* plane to reduce the background noise from multiple interfering modes and remove fixed-term artifacts. Next, we bilaterally zero-padded the spectra to 1024 points and applied an iterative dispersion compensation [38] using Shannon entropy as a sharpness metric [15,39]. Lastly, we inverse Fourier transformed the resulting spectra along the wavenumber axis to obtain a set of 3-D OCT volumes.

After complex OCT image generation, we performed a multi-step volume alignment procedure. In this procedure, each volume is aligned to the first recorded volume. First, we performed an x-y-z alignment based on a 3-D cross-correlation maximization operation in Fourier space (Fig. 3(c)), and then the registered volumes were trimmed to maintain only the overlapping part. Next, we corrected volume rotations around the x- and y-axis (Fig. 3(d)). In this step, we divided
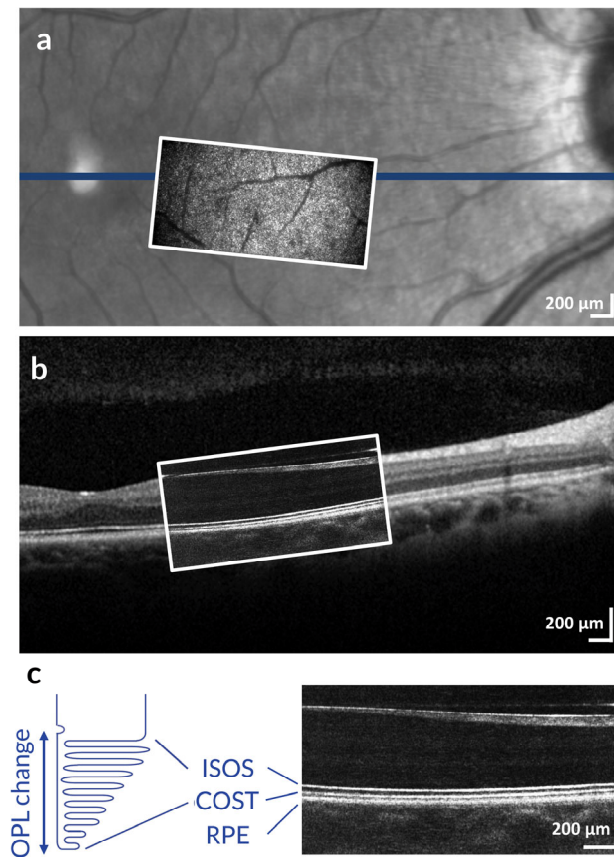
Fig. 2. Location and FOV of the photoreceptor layers involved in the ORG signal detection. (a) *En face* and (b) B-scan structural STOC-T images overlaid on (a) a cSLO fundus image and (b) an SD-OCT B-scan of the subject's retina. (c) Schematic and corresponding STOC-T B-scan showing the location of the IS/OS and COST photoreceptor layers.

each of the consecutive volumes into sub-regions (4×4 pixels in the x-y plane). We estimated the axial shifts of each sub-region for a given volume to the corresponding sub-region in the first volume using a 1-D cross-correlation operation in Fourier space. This operation returned a shift map, which was later fitted by a plane. We used the obtained fit to correct for the volume rotation around the x- and y-axis. This type of correction is simplified as it assumes no transverse shifts for retinal layers (we only perform axial shifts).

After rotation correction, we performed a refined x-y alignment with sub-pixel resolution (Fig. 3(e)), and we also repeated the rotation correction with increased accuracy (Fig. 3(f)). Lastly, for a simplified segmentation of the OCT phase from the photoreceptor layers of interest, we shifted all A-scans in each volume axially by using the Fourier shift theorem to have the IS/OS junction registered at a constant pixel depth. We then multiplied each registered complex volume to the complex conjugate of the first registered volume to cancel any arbitrary phase offset. Next, from the resulting complex-product volumes at every incremental time interval, we segmented two volumes by extracting two manually defined ranges of a few pixels in z, corresponding to the IS/OS and COST layers. Next, we obtained two complex-valued 2-D maps by averaging along the z-axis the two segmented volumes corresponding to the IS/OS and COST layers. We later applied spatial filtering in the x-y plane with a gaussian filter ($\sigma = 3$ pixels) to reduce phase
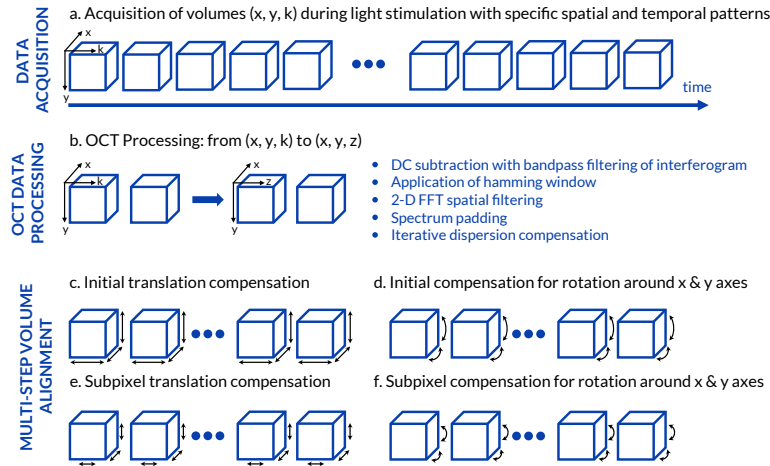
Fig. 3. Schematic illustrating (a) the data acquisition sequence, including synchronized volume acquisition with light stimulation over time; (b) OCT signal processing; and (c-f) multi-step volume alignment procedure – as described in the text.

noise at the expense of a minor resolution degradation, and we then computed the OCT phase difference between the IS/OS and COST layers. Finally, by multiplying the resulting 2-D (x, y) spatially-resolved phase difference by $\lambda_0/(4\pi)$, for every incremental time interval, we obtained the change of photoreceptor OPL over time, and how it varies as a function of light stimulus.

2.3. In vivo human ORG system characterization and experimental protocol

This research was approved by the Bioethical Committee at the Ludwik Rydygier Collegium Medicum of Nicolaus Copernicus University (approval KB 87/2021). It was conducted following the tenets of the Declaration of Helsinki and the internal regulation of the International Centre for Translational Eye Research (ICTER). One subject with no known pathologies was recruited for this study. The subject provided informed consent after the nature and possible risks of the study were explained. Only the subject's right eye was used and the subject's pupil was not dilated for the following experiments.

In the first instance, we checked if the proposed STOC-T system for ORG could detect both the fast contractile (early) and slow swelling (late) response of dark-adapted photoreceptors to a single bright light pulse stimulation, as in [15,19]. For these measurements, the subject's eye was dark adapted for five minutes, and we used a 100 ms light pulse for stimulation. Each dark-adapted period was preceded and followed by the alignment for several seconds of the subject's eye under IR illumination to optimize the OCT signal.

Figure 4 shows the photoreceptor outer segment OPL variation for the fast and slow response, and maps of the spatially-resolved ORG signal for a region at 5° nasal to the fovea. To monitor the fast response a uniform (non-patterned) light pulse stimulus, providing a photon flux of 54×10^2 photons/ms/μm², was used (Fig. 4(a)). Figure 4(b) presents an average of three separate measurements, averaged over a 1.70×0.85 mm² area of the retina, and the photoreceptor OPL change over time shows a negative dip corresponding to the stimulus onset. To monitor the ability to spatially resolve the slow response, a checkerboard-patterned light pulse stimulus, providing a photon flux of 136×10^2 photons/ms/μm², was used.

Figure 4(c) is a map of the late response at 250 ms after the stimulus onset with an average photoreceptor swelling reaching ~150 nm. Lastly, Fig. 4(d) shows an overlay of the late
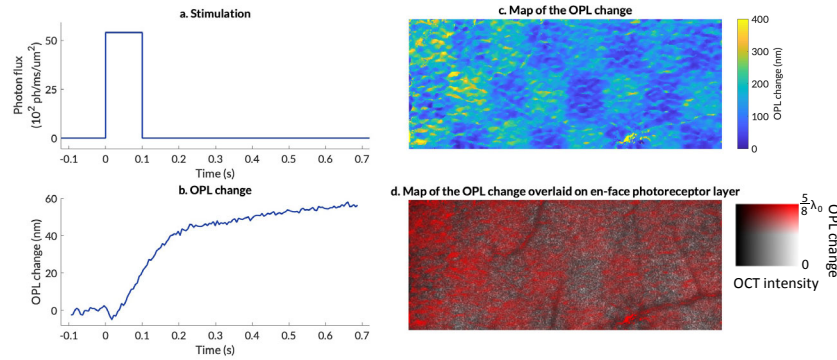
Fig. 4. (a) Onset and duration of a uniform (non-patterned) light pulse stimulus. (b) Photoreceptor OPL change over time (average of three separate measurements) for the light pulse stimulus as of (a) (averaged over a 1.70×0.85 mm^2 area of the retina). (c) Map of a spatially-resolved photoreceptor response to a checkerboard-patterned light pulse stimulus 250 ms after the stimulus onset (with details reported in Table 1.) (d) Overlay of the variation of OPL on a STOC-T *en-face* map showing the photoreceptors layer.

Table 1. Light pulse (flash) ORG experimental parameters.

Figure	Pre-stimulus photon flux (duration ~ 5 min) (10^2 photon/ms/μm^2)	Light pulse peak photon flux (duration: 0.1 s) (10^2 photon/ms/μm^2)	Flickering frequency (Hz)	Spatial averaging (px^2)
4(a)	0	54	0	Whole FOV
4(b), 4(c)	0	136	0	3×3

photoreceptor response (at 250 ms) on a STOC-T *en-face* map of the corresponding photoreceptors layer. Table 1 reports the light pulse (flash) ORG experimental parameters.

We then went on to test our ORG system with a flickering stimulus. The stimulus was a square wave with photon flux oscillating from 0 to I_0 with a 50% duty cycle and one of the following flicker frequencies: 15 Hz, 18 Hz, 20 Hz, 25 Hz, and 30 Hz. We used both uniform and patterned stimuli with alternating dark and flickering stripes, each spanning ~250 μm on the subject's retina.

To overcome the apparent limitation in previous studies [27,28] to measuring fast retinal ORG responses above 10 Hz, we decided to investigate the effect of light-adaptation versus dark-adaptation, as preliminary evidence from experimental work in our laboratory suggested that a period of light adaptation would improve the SNR of the measured photoreceptor modulation amplitude at the flicker frequency. Figure 5 shows how the pre-flickering stimulation influences the measurement results in flicker ORG with a spatially uniform stimulus, flickering at 15 Hz.

The light-adapted pre-flickering protocol included around two minutes dark adaptation interval between measurements followed by one minute pre-flickering illumination with a uniform (non-patterned) stimulus, during which the STOC-T IR light was also on for proper patient alignment. Table 2 reports the system characterization and flicker ORG experimental parameters.

With a very low visible photon flux before the measurement ($I_b = 1.1 \cdot 10^2$ photons/ms/μm^2) in comparison to the peak photon flux during the measurement ($I_0 = 54 \cdot 10^2$ photons/ms/μm^2 - see Fig. 5(a)), bleaching only ~7% of foveal cones after one minute, a significant slow increase in the OPL occurs during the flickering stimulation (Fig. 5(e)). This OPL change is similar to the one observed during the single-pulse stimulation for a dark-adapted eye (Fig. 4(b)). Interestingly, it has a broadband frequency content, which buries the photoreceptor response at 15 Hz in the noise (Fig. 5(i)). We hypothesize it is related to the same physiological mechanism of osmotic
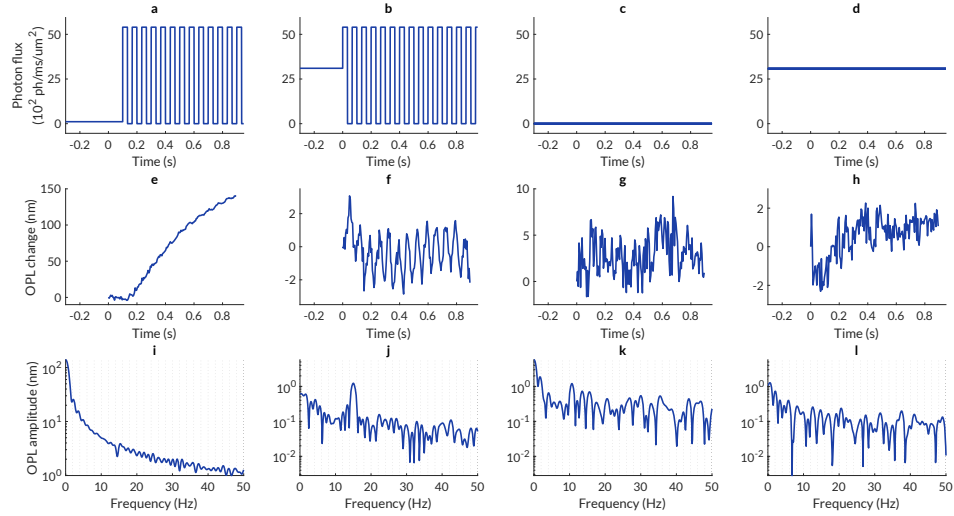
Fig. 5. Comparison of the ORG signals (e)-(h), averaged over the full FOV, and corresponding spectra (i)-(l) obtained under different illumination conditions, represented in (a)-(d). Plots for a dark-adapted eye before flickering stimulation at 15 Hz (a), (e), (i); light-adapted eye before flickering stimulation at 15 Hz (b), (f), (j); no stimulus (c), (g), (k); and constant non-flickering stimulus (d), (h), (l).

Table 2. System characterization and flicker ORG experimental parameters.

Figure	Pre-flickering photon flux (duration ~ 1 min) (10^2 photon/ms/μm^2)	Flickering peak photon flux (duration ~ 0.9 s) (10^2 photon/ms/μm^2)	Flickering frequency (Hz)	Spatial averaging (px^2)
5(a), 6(a)	1.1	54	15	Whole FOV
5(b), 6(b), 7(a)	31	54	15	Whole FOV
5(c)	0	N/A	0	Whole FOV
5(d)	31	N/A	0	Whole FOV
7(b)	31	54	20	Whole FOV
7(c)	31	54	25	Whole FOV
7(d)	31	54	30	Whole FOV
8(a)	13	13	0 & 15, stripes	3×3
8(b)	12	12	0 & 15 & 18, stripes	3×3

changes in the photoreceptors, generated as by-products of the phototransduction process in a dark-adapted eye [16], as the pre-flickering photon flux is very low, and, therefore, we shall refer to this case as "dark adapted" in the rest of the manuscript for simplicity.

When, instead, we used a stronger visible photon flux before the measurement ($I_b = 31 \cdot 10^2$ photons/ms/μm^2) equal to roughly half the peak photon flux during the measurement ($I_0 = 54 \cdot 10^2$ photons/ms/μm^2 – see Fig. 5(b)), bleaching ~81% of foveal cones after one minute, the slow swelling of the photoreceptors was not observed, whilst the photoreceptor OPL change at a given flickering frequency became visible in the stimulated retinal regions (Fig. 5(f)). The photoreceptor OPL modulation amplitude at 15 Hz was ~1 nm and it stands out from the background noise (Fig. 5(j)).

2.4. Flicker ORG: displacement sensitivity and OPL modulation amplitude sensitivity

To characterize the OPL modulation amplitude sensitivity of our flicker ORG system, we acquired first a benchmarking measurement on an eye phantom (OCT Model Eye, Rowe Technical Design), where no flicker and no eye motion were present. To perform a cleaner frequency analysis of the detected signals, we applied a high-pass filter (> 10 Hz), from the MATLAB built-in "highpass" function, which removed the slow OPL variations.

The STOC-T displacement sensitivity was experimentally calculated as the standard deviation over time of the high-passed OPL difference between two retinal phantom layers, averaged over the x-y plane in the FOV, and it was 0.25 nm. However, as the phase noise was distributed rather evenly in the bandwidth of interest (10-50 Hz), the mean noise amplitude in the frequency spectrum was only 40 pm with a standard deviation of 30 pm.

We then acquired and analyzed the ORG signal *in vivo* when there was no stimulation (Figs. 5(c), 5(g)) and when a constant stimulation (Figs. 5(d)–5(h)) with a photon flux of $I_b = 31 \cdot 10^2$ photons/ms/μm^2 was provided, *i.e.*, the light was not modulated in time, as control cases. For ORG measurements without stimulation, the standard deviation of the high-passed OPL change over time was 2.12 nm. However, as in the phantom eye case, in the bandwidth of interest (10-50 Hz – Fig. 5(k)), the mean value of the amplitude spectrum was roughly an order of magnitude smaller, namely 340 pm, with a standard deviation equal to 210 pm. In the case of constant illumination on the retina, a slight improvement was also noticed, as the standard deviation of the high-passed OPL change over time was 0.83 nm, and the mean value of the spectrum was 140 pm with a standard deviation equal to 90 pm.

For comparison to theoretical predictions, we computed from Eq. (2) the STOC-T theoretical best displacement sensitivity from the theoretical phase difference sensitivity $\sigma_{\Delta\varphi}$, [40,41], as

$$d_{\Delta\varphi} = \lambda_0 \frac{\sigma_{\Delta\varphi}}{4\pi}. \tag{2}$$

The theoretical best phase difference sensitivity $\sigma_{\Delta\varphi}$ [18,42], is inversely related to a composite SNR arising from the differential SNRs of the two retinal layers of interest, $SNR(z_1, t)$ and $SNR(z_2, t)$, as follows in Eq. (3):

$$\sigma_{\Delta\varphi} = \sqrt{\frac{SNR(z_1, t) + SNR(z_2, t)}{2 \cdot SNR(z_1, t)SNR(z_2, t)}}. \tag{3}$$

In the case of constant illumination on the retina (Fig. 5(d)), the IS/OS layer had an average OCT $SNR(z_1, t) = 9$ dB, while the COST layer had an average OCT $SNR(z_2, t) = 10.6$ dB. Therefore, the composite OCT SNR from the two layers is 9.7 dB for any given (x,y) position in the FOV. However, there are N independent depth scans to be averaged, where $N = 512 \times 256 = 131,072$ pixels in an x-y plane. Averaging would improve the SNR by a factor of $\sqrt{N}$ [43], leading to an SNR = 35.3 dB, which corresponds to a theoretical displacement sensitivity $d_{\Delta\varphi} = 1.1$ nm. The measured STOC-T displacement sensitivity of 0.83 nm is consistent with a theoretical displacement sensitivity of 1.1 nm, when considering that the experimental one comes from a high-passed filtered measurement. Ultimately though, the OPL modulation amplitude sensitivity for flicker ORG *in vivo* is determined by the noise floor in the frequency domain, which is 140 pm for this case.

In Fig. 6, we show the measured changes in OPL, averaged from the whole FOV, to the uniform (non-patterned) stimulus flickering at 15 Hz for both the dark-adapted (Fig. 5(a)) and light-adapted (Fig. 5(b)) eye, after applying the high-pass filter. These signals were obtained from separate measurements and averaged among them. Figure 6(a) shows the high pass-filtered dark-adapted ORG signal in red, while Fig. 6(b) shows the high pass-filtered light-adapted ORG signal in blue, and the unfiltered light-adapted ORG signal dashed in black, as in Fig. 5(f) for reference.

Figure 6(c)–6(d) shows the corresponding modulation amplitude spectra, with the same color code as in Figs. 6(a)–6(b). Despite the filtering operation reduces the low-frequency noise and it brings out a peak at 15 Hz, previously invisible for the dark-adapted eye in Fig. 5(i), it is evident that the dark-adapted signal presents higher background noise even at higher frequencies.
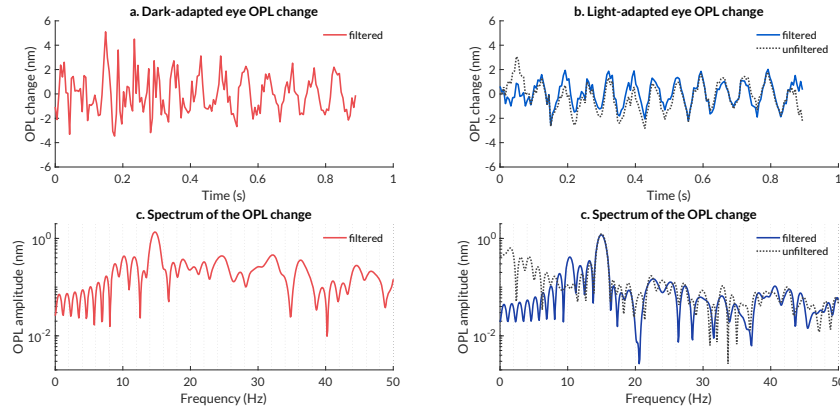

Fig. 6. Averaged measured filtered ORG response and OPL modulation amplitude spectrum to a 15 Hz stimulus. (a) Averaged, dark-adapted ORG signal, as in Fig. 5(e), after high pass-filtering in solid red. (b) Averaged, light-adapted ORG signal, as in Fig. 5(f) in a black dashed line and after high pass-filtering in solid blue. (c) Modulation amplitude spectrum of the ORG signal in (a). (d) Modulation amplitude spectrum of the ORG signals in (b). The FFT is zero-padded to N = 2048 datapoints. The OPL modulation amplitude spectrum is computed as the amplitude spectrum of the zero-padded signal normalized by half the raw number of time steps (bins).

To objectively quantify the superior performance of the light-adapted pre-flickering protocol in teasing out the photoreceptor OPL modulation response, we then compared the OPL modulation SNR values, where the signal is evaluated as the peak value at 15 Hz while the noise is evaluated as the root mean square in the 18-50 Hz range.

We obtained an average OPL modulation SNR equal to 13.91 dB with a standard deviation of 0.23 dB for the low pre-flickering photon flux (dark-adapted case). The average OPL modulation SNR value increased to 25.29 dB with a standard deviation of 1.79 dB with the higher pre-flickering photon flux (light-adapted case). As such, during flicker ORG experiments, no dark adaptation was required, and, subsequently, we set a pre-flicker illumination with a photon flux above $12 \cdot 10^2$ photons/ms/μm^2.

3. Results

Figure 7 shows the photoreceptor OPL modulation amplitude spectra from several high-pass-filtered ORG measurements, averaged in the whole FOV in a region at 5° nasal to the fovea, in response to a uniform (non-patterned) flickering stimulus under the light-adapted protocol.

The flickering frequencies we used were 15 Hz, 20 Hz, 25 Hz, and 30 Hz, respectively. We repeated these measurements several times for each flickering frequency and computed the mean spectra (in a solid blue line) and the corresponding ± one standard deviation range (in a blue shade) from a total of eight (Fig. 7(a)), six (Fig. 7(b)), six (Fig. 7(c)), and five spectra (Fig. 7(d)).

We then extracted the peak amplitude values from each measurement for each flickering frequency (see means and standard deviations in Table 3) and ran several two-sample t-Tests on the peak amplitude samples from different flickering frequency pairs to test if the corresponding normal distributions have statistically different mean peak amplitudes (p-value < 5%). The
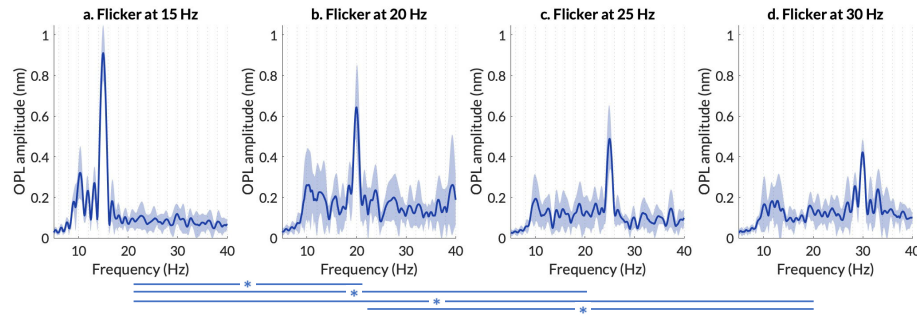
Fig. 7. Spectra of OPL modulation amplitude resulting from a spatially-uniform, flickering stimulation with a frequency of (a) 15 Hz, (b) 20 Hz, (c) 25 Hz, and (d) 30 Hz, under light-adapted protocol as in Fig. 5(b). Each plot shows the average (in a solid blue line) and the ± one standard deviation range (in a blue shade) for (a) eight, (b) six, (c) six, and (d) five high pass-filtered ORG measurement spectra. At the bottom of the graphs, the horizontal lines and the asterisks (*) join the pairs of datasets from different flickering frequencies that have statistically different mean peak modulation amplitudes.

results showed that the pairs (15 Hz – 20 Hz), (15 Hz – 25 Hz), (15 Hz – 30 Hz), and (20 Hz – 30 Hz) all have statistically different mean peak amplitudes (see Table 4) in response to the corresponding flickering stimuli, with a trend of decreasing amplitude with increasing flickering frequency.

Table 3. Mean and standard deviation of peak values for the datasets presented in Fig. 7.

Frequency	Mean peak value (nm)	Standard deviation (nm)
15 Hz	0.90	0.13
20 Hz	0.64	0.20
25 Hz	0.48	0.15
30 Hz	0.42	0.06

Table 4. Results of the statistical significance test (p values) for the datasets presented in Fig. 7.

20 Hz	25 Hz	30 Hz	p-values
0.73%	0.012%	0.001%	15 Hz
	12%	2.7%	20 Hz
		40%	25 Hz

The plots not only show that the measured responses follow the stimulus frequency, as expected, but also a statistically-significant decreasing photoreceptor OPL modulation amplitude with increasing flicker frequencies, hinting at the approaching CFF [44].

Next, we mapped the photoreceptor OPL change in response to striped-patterned stimuli to highlight the technical ability of our system and experimental protocol to spatially map the response to different flickering frequencies over a large FOV on one side, and the potential to study the spatial distribution of the temporal frequency response of photoreceptors OPL changes on the other, providing complementary information to flicker ERG studies and with higher resolution. For this work, we replaced the high-pass filter with a 1 Hz band-pass filter to isolate

the modulation signal in the band of interest. Then we calculated the average peak modulation by averaging the modulation envelope values estimated using the Hilbert transform.

Figure 8(a) shows the measurement of the photoreceptor OPL modulation amplitude in response to a stimulus with stripes flickering at 15 Hz. Figure 8(b), instead, shows the measurement of the photoreceptor OPL change in response to a stimulus containing stripes where every second flickering one was set at a frequency of 15 Hz and 18 Hz, respectively.
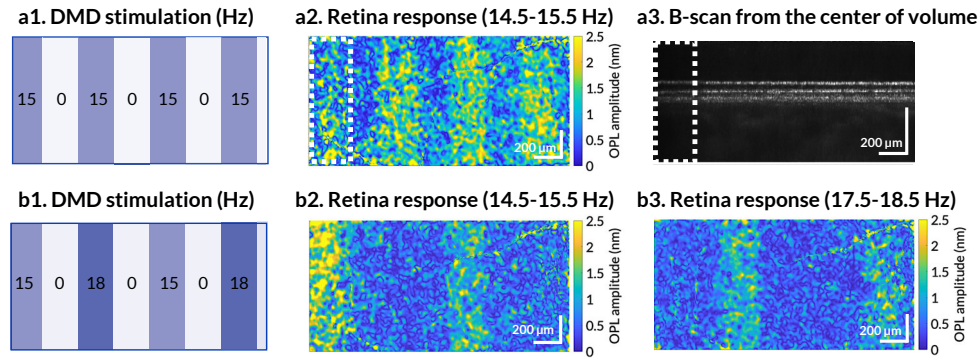

Fig. 8. Measured photoreceptor OPL modulation amplitude in response to a patterned flickering white light stimulation. (a) Measured ORG response to stimulation with a pattern containing 15 Hz flickering stripes. Pre-flicker photon flux of $13 \cdot 10^2$ photons/ms/μm^2, flickering peak photon flux $I_0 = 13 \cdot 10^2$ photons/ms/μm^2. (b) Measured ORG response to stimulation with a pattern containing alternately 15 Hz and 18 Hz flickering stripes (see Visualization 1). Pre-flicker photon flux of $12 \cdot 10^2$ photons/ms/μm^2 flickering peak photon flux $I_0 = 12 \cdot 10^2$ photons/ms/μm^2.

We can observe how the regions corresponding to a stimulus stripe flickering at 15 Hz present higher amplitude of the OPL change than those at 18 Hz, while the control regions showed no signal. Visualization 1 shows a video of the spatially-resolved photoreceptor OPL modulation amplitude in response to the stimulus of Fig. 8(b) in different frequency bands, with a rolling band-pass filter with a bandwidth of 1 Hz, overlaid on an *en-face* STOC-T image of the corresponding photoreceptor layer.

4. Discussion

We demonstrated the ability of our flicker ORG system to spatially detect the photoreceptor response to a patterned stimulus with light stripes flickering at different frequencies. Despite the limits to the achievable OCT SNR, brought by the outstanding temporal resolution of STOC-T for volumetric imaging (5.32 ms) together with the low retinal irradiance from the IR light source, a good phase sensitivity and hence displacement sensitivity was achieved thanks to a sub-pixel 5 degree-of-freedom volume registration and spatial averaging (when performed) post-processing procedure and the likely advantage offered by the effective scattering crosstalk reduction in our STOC-T system.

In fact, our STOC-T system presents a displacement sensitivity in the order of 830 pm *in vivo*. However, flicker ORG additionally benefits from the SNR improvement brought by frequency modulation of the photoreceptor OPL change signal. Therefore, detection of OPL modulation amplitudes above 40 pm if no eye motion is attained, and above 140 pm for *in vivo* fixated eyes are possible with our system. This performance improvement is similar to that achieved with other phase-sensitive OCT systems that modulate the signal in frequency [45–47]. This approach allowed us to map both the early and late response of photoreceptors to light pulse stimulation as well as the tiny photoreceptor OPL modulation amplitudes over a broad range of frequencies

below the CFF. While we have shown statistically significant differences in photoreceptor OPL modulation amplitudes at different flicker frequencies in a retinal region 5° nasal to the fovea in one volunteering subject, it is important to be aware of potential inter-subject variability for any study on vision or clinical applications.

For the *in vivo* case, a better sensitivity (140 pm versus 340 pm) to the photoreceptor OPL modulation amplitude was attained with a constant illumination rather than in the dark (Figs. 5(h)–5(l) versus Figs. 5(g)–5(k)), possibly owing to better fixation and therefore less motion artifacts when fixation happened via the measured eye rather than via the fellow eye, as in the dark case.

Additionally, the ORG system detected OPL modulations in the stimulated bands with reasonably higher SNR when a light-adapted eye, rather than a dark-adapted eye, was exposed to the flickering stimulus. Therefore, the pre-flicker illumination was instrumental in preconditioning the photoreceptors OPL variation, by reducing the concurrent slow swelling and the associated broadband frequency content contributing to the background noise. As such, the measured photoreceptor modulation amplitude at a given flicker frequency was detected against a lower noise background. In fact, in light-adapted conditions, the typical swelling of the slow ORG response, associated with the physiological mechanism of osmotic changes in the photoreceptors, generated as by-products of the phototransduction process in a dark-adapted eye, was no longer visible. Future studies will aim to relate this effect to the underlying physiological mechanism.

In this manuscript, we presented the photoreceptor OPL frequency response at selected frequencies in a range above the frequencies currently presented in the literature up to just above video rates (30 Hz). However, it is feasible to perform such experiments at lower and higher frequencies. The limits to the achievable frequency range are the following: at higher frequencies, the ultimate limit is the photoreceptor OPL modulation amplitude sensitivity, *i.e.*, we cannot detect modulation amplitudes smaller than 140 pm, which already requires spatially averaging the ORG signal over a significant portion of the retina due to the limited OCT SNR of our system; at lower frequencies, we are limited by the number of signal periods that we can acquire in one measurement (although this could be solved by reducing the volume sampling rate) and by the increasing phase noise produced by eye motion over longer acquisitions (even after volume co-registration).

Slightly imperfect volume co-registrations, especially when residual off-center tilts are present, could be the reason why we observed a photoreceptor OPL variation gradient in Fig. 4(b). Further improvements to the volume co-registration procedure would be sought after to guarantee artifact-free OPL change maps. The apparent absence of response towards the left edge of the map in Fig. 8(a) can be attributed to a reduction in recorded OCT intensity, as visible in the B-scan, and it is due to vignetting by the iris. As the pupil in those experiments was not dilated, pupillary contraction with pre-flickering and flickering light posed an increasing strain on eye centration, and, at times, it resulted in vignetted data. A potential future solution would be to use topical mydriatics for pupil dilation before ORG.

Additionally, some of the edges of the detected patterns are blurred. This issue is partially caused by a lack of synchronization between the projected pattern and the eye position, as the pattern position on the retina changes during data acquisition due to eye movement. This problem might be solved in future by integrating real-time eye tracking into the system [48] to shift the position of the stimulus pattern accordingly. Such a solution might be needed for ORG tests with higher spatial frequency patterns.

An alternative cause for the observed blur might be the optical aberrations in the subject's eye, which reduce the sharpness of the projected pattern on the retina. Implementation of hardware adaptive optics methods [49], especially those suited to full-field OCT [50], will certainly enable better pattern delineation in the response by the photoreceptor layer, and even single-photoreceptor ORG by tracking them within the photoreceptor mosaic.

5. Conclusions

In conclusion, we demonstrated that we could detect the photoreceptor response to different flicker frequencies in a repeatable fashion with a STOC-T system and with improved SNR thanks to a light-adapted experimental protocol. We also demonstrated the ability to spatially detect the response to a patterned stimulus with light stripes flickering at different frequencies. These results highlight the prospect for a more objective study of CFF variations across the retina or complete characterization of the spatially-resolved temporal-frequency response of the retina with flicker ORG perimetry and other novel accurate retinal functional studies for early detection of retinal degeneration and therapy monitoring.

Disclosures. The authors declare no conflicts of interest.

Data availability. Data underlying the results presented in this paper are not publicly available at this time but may be obtained from the authors upon reasonable request.

References

1. L. A. Yannuzzi, M. D. Ober, J. S. Slakter, R. F. Spaide, Y. L. Fisher, R. W. Flower, and R. Rosen, "Ophthalmic fundus imaging: today and beyond," Am. J. Ophthalmol. **137**(3), 511–524 (2004).
2. J. F. de Boer, R. Leitgeb, and M. Wojtkowski, "Twenty-five years of optical coherence tomography: the paradigm shift in sensitivity and speed provided by Fourier domain OCT [Invited]," Biomed. Opt. Express **8**(7), 3248–3280 (2017).
3. R. S. Jonnal, "Toward a clinical optoretinogram: a review of noninvasive, optical tests of retinal neural function," Ann. Transl. Med. **9**(15), 1270 (2021).
4. P. Gouras, "Symposium on Electrophysiology: Electroretinography: Some Basic Principles," Invest. Ophthalmol. Visual Sci. **9**, 557–569 (1970).
5. E. E. Sutter and D. Tran, "The field topography of ERG components in man—I. The photopic luminance response," Vision Res. **32**(3), 433–446 (1992).
6. X.-C. Yao, A. Yamauchi, B. Perry, and J. S. George, "Rapid optical coherence tomography and recording functional scattering changes from activated frog retina," Appl. Opt. **44**(11), 2019–2023 (2005).
7. K. Bizheva, R. Pflug, B. Hermann, B. Považay, H. Sattmann, P. Qiu, E. Anger, H. Reitsamer, S. Popov, J. R. Taylor, A. Unterhuber, P. Ahnelt, and W. Drexler, "Optophysiology: Depth-resolved probing of retinal physiology with functional ultrahigh-resolution optical coherence tomography," Proc. Natl. Acad. Sci. U. S. A. **103**(13), 5066–5071 (2006).
8. V. J. Srinivasan, M. Wojtkowski, J. G. Fujimoto, and J. S. Duker, "In vivo measurement of retinal physiology with high-speed ultrahigh-resolution optical coherence tomography," Opt. Lett. **31**(15), 2308–2310 (2006).
9. R. S. Jonnal, J. Rha, Y. Zhang, B. Cense, W. Gao, and D. T. Miller, "In vivo functional imaging of human cone photoreceptors," Opt. Express **15**(24), 16141–16160 (2007).
10. K. Grieve and A. Roorda, "Intrinsic Signals from Human Cone Photoreceptors," Invest. Ophthalmol. Visual Sci. **49**(2), 713–719 (2008).
11. J. B. Mulligan, D. I. MacLeod, and I. C. Statler, "In search of an optoretinogram," (1994).
12. X. Yao and B. Wang, "Intrinsic optical signal imaging of retinal physiology: a review," J. Biomed. Opt. **20**(9), 090901 (2015).
13. R. F. Cooper, D. H. Brainard, and J. I. W. Morgan, "Optoretinography of individual human cone photoreceptors," Opt. Express **28**(26), 39326–39339 (2020).
14. M. Azimipour, D. Valente, K. V. Vienola, J. S. Werner, R. J. Zawadzki, and R. S. Jonnal, "Optoretinogram: optical measurement of human cone and rod photoreceptor responses to light," Opt. Lett. **45**(17), 4658–4661 (2020).
15. D. Hillmann, H. Spahr, C. Pfäffle, H. Sudkamp, G. Franke, and G. Hüttmann, "In vivo optical imaging of physiological responses to photostimulation in human photoreceptors," Proc. Natl. Acad. Sci. **113**(46), 13138–13143 (2016).
16. P. Zhang, R. J. Zawadzki, M. Goswami, P. T. Nguyen, V. Yarov-Yarovoy, M. E. Burns, and E. N. Pugh, "In vivo optophysiology reveals that G-protein activation triggers osmotic swelling and increased light scattering of rod photoreceptors," Proc. Natl. Acad. Sci. **114**(14), E2937–E2946 (2017).
17. F. Zhang, K. Kurokawa, A. Lassoued, J. A. Crowell, and D. T. Miller, "Cone photoreceptor classification in the living human eye from photostimulation-induced phase dynamics," Proc. Natl. Acad. Sci. **116**(16), 7951–7956 (2019).

18. V. P. Pandiyan, X. Jiang, A. Maloney-Bertelli, J. A. Kuchenbecker, U. Sharma, and R. Sabesan, "High-speed adaptive optics line-scan OCT for cellular-resolution optoretinography," Biomed. Opt. Express **11**(9), 5274–5296 (2020).

19. V. P. Pandiyan, A. Maloney-Bertelli, J. A. Kuchenbecker, K. C. Boyle, T. Ling, Z. C. Chen, B. H. Park, A. Roorda, D. Palanker, and R. Sabesan, "The optoretinogram reveals the primary steps of phototransduction in the living human eye," Sci. Adv. **6**(37), eabc1124 (2020).

20. K. C. Boyle, Z. C. Chen, T. Ling, V. P. Pandiyan, J. Kuchenbecker, R. Sabesan, and D. Palanker, "Mechanisms of Light-Induced Deformations in Photoreceptors," Biophys. J. **119**(8), 1481–1488 (2020).

21. X. Yao and T.-H. Kim, "Fast intrinsic optical signal correlates with activation phase of phototransduction in retinal photoreceptors," Exp. Biol. Med. **245**(13), 1087–1095 (2020).

22. P. Zhang, B. Shibata, G. Peinado, R. J. Zawadzki, P. FitzGerald, and E. N. Pugh Jr, "Measurement of Diurnal Variation in Rod Outer Segment Length In Vivo in Mice With the OCT Optoretinogram," Invest. Ophthalmol. Visual Sci. **61**(3), 9 (2020).

23. T.-H. Kim, B. Wang, Y. Lu, T. Son, and X. Yao, "Functional optical coherence tomography enables in vivo optoretinography of photoreceptor dysfunction due to retinal degeneration," Biomed. Opt. Express **11**(9), 5306–5320 (2020).

24. S. Wu and S. A. Burns, "Analysis of retinal light adaptation with the flicker electroretinogram," J. Opt. Soc. Am. A **13**(3), 649–657 (1996).

25. W. Seiple and K. Holopigian, "Outer-retina locus of increased flicker sensitivity of the peripheral retina," J. Opt. Soc. Am. A **13**(3), 658–666 (1996).

26. T. Schmoll, C. Kolbitsch, and R. Leitgeb, "In vivo functional retinal optical coherence tomography," J. Biomed. Opt. **15**(4), 041513 (2010).

27. C. Pfäffle, H. Spahr, L. Kutzner, S. Burhan, F. Hilge, Y. Miura, G. Hüttmann, and D. Hillmann, *Functional imaging of neuronal layers in the human retina (Conference Presentation)*, SPIE BiOS (SPIE, 2020), Vol. 11228.

28. C. Pfäffle, H. Spahr, K. Gercke, S. Burhan, D. Melenberg, Y. Miura, G. Hüttmann, and D. Hillmann, *Phase-sensitive measurements of depth dependent signal transduction in the inner plexiform layer*, SPIE BiOS (SPIE, 2021), Vol. 11623.

29. E. Auksorius, D. Borycki, P. Węgrzyn, B. L. Sikorski, I. Zickiene, K. Lizewski, M. Rapolu, K. Adomavicius, S. Tomczewski, and M. Wojtkowski, "Spatio-Temporal Optical Coherence Tomography provides advanced imaging of the human retina and choroid," arXiv preprint arXiv:2107.10672 (2021).

30. E. Auksorius, D. Borycki, P. Węgrzyn, I. Žičkienė, K. Adomavičius, B. L. Sikorski, and M. Wojtkowski, "Multimode fiber as a tool to reduce cross talk in Fourier-domain full-field optical coherence tomography," Opt. Lett. **47**(4), 838–841 (2022).

31. D. Borycki, M. Hamkało, M. Nowakowski, M. Szkulmowski, and M. Wojtkowski, "Spatiotemporal optical coherence (STOC) manipulation suppresses coherent cross-talk in full-field swept-source optical coherence tomography," Biomed. Opt. Express **10**(4), 2032–2054 (2019).

32. E. Auksorius, D. Borycki, and M. Wojtkowski, "Multimode fiber enables control of spatial coherence in Fourier-domain full-field optical coherence tomography for in vivo corneal imaging," Opt. Lett. **46**(6), 1413–1416 (2021).

33. W. A. H. Rushton and G. H. Henry, "Bleaching and regeneration of cone pigments in man," Vision Res. **8**(6), 617–631 (1968).

34. W. A. H. Rushton, "Visual Pigments in Man," in *Photochemistry of Vision*, H. J. A. Dartnall, ed. (Springer Berlin Heidelberg, Berlin, Heidelberg, 1972), pp. 364–394.

35. J. L. Miller, E. Friedman, J. N. Sanders-Reed, K. Schwertz, and B. K. McComas, *Photonics rules of thumb*, Third ed. (SPIE Press, 2020).

36. E. Auksorius, "Fourier-domain full-field optical coherence tomography with real-time axial imaging," Opt. Lett. **46**(18), 4478–4481 (2021).

37. E. Auksorius, D. Borycki, and M. Wojtkowski, "Crosstalk-free volumetric in vivo imaging of a human retina with Fourier-domain full-field optical coherence tomography," Biomed. Opt. Express **10**(12), 6390–6407 (2019).

38. M. Wojtkowski, V. J. Srinivasan, T. H. Ko, J. G. Fujimoto, A. Kowalczyk, and J. S. Duker, "Ultrahigh-resolution, high-speed, Fourier domain optical coherence tomography and methods for dispersion compensation," Opt. Express **12**(11), 2404–2422 (2004).

39. B. Flores, *Robust method for the motion compensation of ISAR imagery*, Robotics '91 (SPIE, 1992), Vol. 1607.

40. B. Hyle Park, M. C. Pierce, B. Cense, S.-H. Yun, M. Mujat, G. J. Tearney, B. E. Bouma, and J. F. D. Boer, "Real-time fiber-based multi-functional spectral-domain optical coherence tomography at 1.3 µm," Opt. Express **13**(11), 3931–3944 (2005).

41. L. Chin, A. Curatolo, B. F. Kennedy, B. J. Doyle, P. R. T. Munro, R. A. McLaughlin, and D. D. Sampson, "Analysis of image formation in optical coherence elastography using a multiphysics approach," Biomed. Opt. Express **5**(9), 2913–2930 (2014).

42. M. Q. Tong, M. M. Hasan, S. S. Lee, M. R. Haque, D.-H. Kim, M. S. Islam, M. E. Adams, and B. H. Park, "OCT intensity and phase fluctuations correlated with activity-dependent neuronal calcium dynamics in the Drosophila CNS [Invited]," Biomed. Opt. Express **8**(2), 726–735 (2017).

43. B. Baumann, C. W. Merkle, R. A. Leitgeb, M. Augustin, A. Wartak, M. Pircher, and C. K. Hitzenberger, "Signal averaging improves signal-to-noise in OCT images: But which approach works best, and when?" Biomed. Opt. Express **10**(11), 5755–5775 (2019).

44. E. Hartmann, B. Lachenmayr, and H. Brettel, "The peripheral critical flicker frequency," Vision Res. **19**(9), 1019–1023 (1979).

45. D. C. Adler, S.-W. Huang, R. Huber, and J. G. Fujimoto, "Photothermal detection of gold nanoparticles using phase-sensitive optical coherence tomography," Opt. Express **16**(7), 4376–4393 (2008).

46. R. Wang and A. Nuttall, "Phase-sensitive optical coherence tomography imaging of the tissue motion within the organ of Corti at a subnanometer scale: a preliminary study," J. Biomed. Opt. **15**(5), 056005 (2010).

47. S. Kim, J. S. Oghalai, and B. E. Applegate, "Noise and sensitivity in optical coherence tomography based vibrometry," Opt. Express **27**(23), 33333–33350 (2019).

48. F. Feroldi, S. Mozaffari, F. LaRocca, P. K. Tiruveedhula, P. Gregory, B. H. Park, and A. J. Roorda, "Optoretinography in the human retina using AOOCT and AOSLO-based eye tracking," Invest. Ophthalmol. Visual Sci. **62**, 28 (2021).

49. M. Pircher and R. J. Zawadzki, "Review of adaptive optics OCT (AO-OCT): principles and applications for retinal imaging [Invited]," Biomed. Opt. Express **8**(5), 2536–2562 (2017).

50. J. Scholler, K. Groux, K. Grieve, C. Boccara, and P. Mecê, "Adaptive-glasses time-domain FFOCT for wide-field high-resolutionretinal imaging with increased SNR," Opt. Lett. **45**(21), 5901–5904 (2020).